Prism matching for piston segmentation correction with adaptive optics systems on extremely large telescopes

Richard M. Clare, Byron E. Engler, Stephen J. Weddell
Department of Electrical and
Computer Engineering,
University of Canterbury,
Private Bag 4800
Christchurch 8020, New Zealand
Email: richard.clare@canterbury.ac.nz

Miska Le Louarn, Christophe Vérinaud
Adaptive Optics Group
European Southern Observatory
Karl-Schwarzschild Straße 2,
Garching bei Müenchen, Germany

Abstract—Images observed at ground-based telescopes are blurred by Earth's atmosphere. Adaptive optics systems can correct for this blurring by using a wavefront sensor to measure the instantaneous wavefront aberration created by the atmosphere, and a deformable mirror to apply correction to the aberrated wavefront. The European Extremely Large Telescope, one of the next generation of telescopes currently under construction, will have large supporting struts or arms (spiders) for the secondary mirror that obscure whole rows and columns of subapertures in the wavefront sensor. This phase discontinuity can allow large segment piston errors to arise between neighbouring segments, because the deformable mirror can produce the segment modes but the wavefront sensor senses them poorly. The spider for the EELT will have six arms, and we propose in this paper employing a six-sided prism for the wavefront sensor instead of the traditional four sided pyramid. We show that when the diffraction spikes from the spider arms are aligned in the middle of the prism faces, the sensitivty of the sensor, as measured by the sum of the singular values of the interaction matrix for the six segment piston modes, is 15% larger than if the diffraction spikes are aligned with the prism edges.

I. INTRODUCTION

Images of astronomical objects that are observed from ground-based telescopes are distorted by Earth's atmosphere [1]. One method to overcome these distortions is to employ an Adaptive Optics (AO) system [2]. An AO system, as shown in Figure 1, operates by employing a wavefront sensor (WFS) to estimate the wavefront aberration induced by the time-varying atmosphere, and a deformable mirror (DM) to apply a correction to overcome this wavefront aberration.

We are entering the era of extremely large telescopes, which are telescopes of primary mirror diameters of 25 m-40 m, all of which will be equipped with AO systems. Currently, under construction are the Thirty Meter Telescope [4], Giant Magellan Telescope [5], and the European Extremely Large Telscope (EELT) [6]. We will concentrate on the latter in this paper.
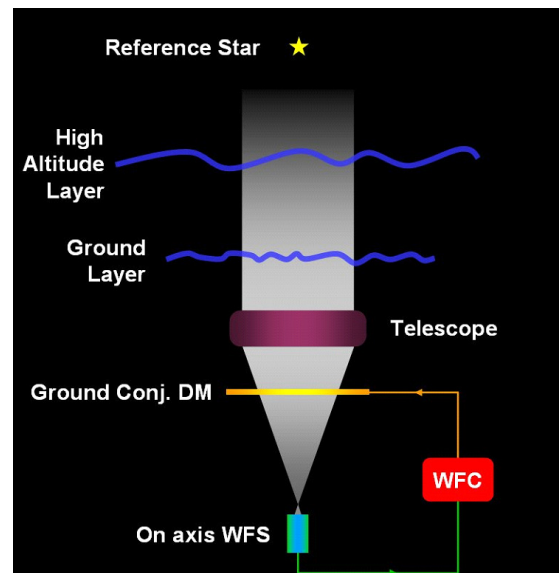

Fig. 1. In an adaptive optics system, a wavefront controller (WFC) takes wavefront measurements from a wavefront sensor (WFS) and calculates corrections to apply to a deformable mirror (DM) to correct for the effects of Earth's atmosphere on astronomical images [3].

Several different WFS exist in AO systems around the world, but the most popular for the design of the ELTs is the pyramid wavefront sensor [7]–[9]. The pyramid WFS, shown in Figure 2, consists of a glass pyramid that subdivides the complex field at the focal plane into quadrants, and the light subsequently passes through a relay lens to form four images of the aperture. The slope of the wavefront can then be calculated from these four images from geometric considerations. Additionally, the pyramid wavefront sensor can be modulated by moving the spot at the focal plane about the vertex of the pyramid. This increases the dynamic range of the measurements, but at a cost of reduced sensitivity.

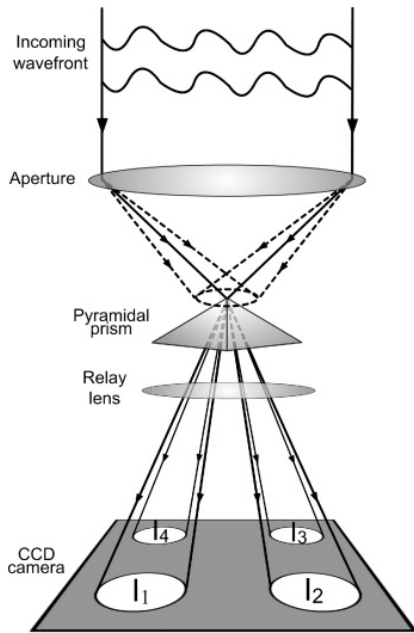The pyramid is actually one of a class of sensors that divide

Fig. 2. The pyramid wavefront sensor operates by subdividing the light at the focal plane into four quadrants with a 4-sided glass prism. Subsequently, the light passes through a relay lens to form four images of the aperture $I(x, y)$. The pyramid can be modulated by moving the light around the vertex of the pyramid as indicated by the dotted circle. [10]

Fig. 3. The six segment piston modes for a six-arm spider (rotation angle θ of 0°) on the EELT [16].

Fig. 4. The residual optical path difference in a closed loop adaptive optics simulation for the EELT [14].

the focal plane of the telescope into N segments with an N-sided prism, and producing N aperture images [11]. For a circular unobstructed aperture, analytical derivations have shown that the performance of the WFS is largely independent of the number of sides of the prism [12]. Simulation studies have shown similar performance of the 3, 4, 6 and two 2-sided prisms for the EELT [13].

The secondary mirror of the EELT is itself very large, and requires large support beams (width of $50\,\mathrm{cm}$ [14]) to hold it in place. These support beams, commonly known as spiders, have the effect of masking whole rows and columns of subapertures of the pyramid WFS images. Because the width of these spider arms is greater than the typical coherence length of the atmosphere r_0 of typically 10-20 cm, the AO reconstructor can develop large piston segment errors [15]. In optics, piston is a constant phase across the pupil, and a piston segment is a constant phase across a segment of the pupil. The six segment piston modes that arise for a six-arm spider pupil $P(x, y)$ are shown in Figure 3. These segment piston errors arise because the DM can generate the shapes of the six segment piston modes, but the modulated pyramid WFS is largely insensitive to these modes. A simulation of the AO system for the EELT shows these segment piston errors developing, as shown by the residual optical path difference in Figure 4 [14]. These segment piston errors can reduce the image quality, as measured by the Strehl metric (the ratio of the peak of the aberrated point spread function to the peak of the diffraction-limited point spread function), on the EELT by as much as 50% [15].
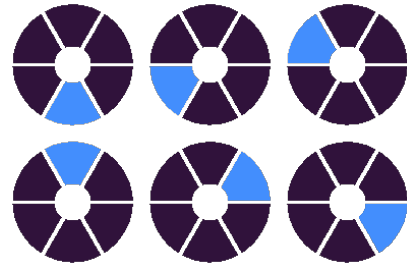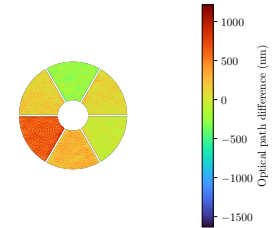
The unmodulated (static) pyramid wavefront sensor has been shown to be significantly more sensitive to the piston segment modes than its modulated counterpart [16]. In Ref. 17, the authors show that it is possible to measure and correct for piston segment errors in the near infra-red K-Band ($2.2\,\mathrm{\mu m}$), by having two independent reconstructors, one to correct the atmospheric modes and one to correct the piston sgement modes only. These ideas are further elaborated in Ref. 14, where a pyramid with alternating states (modulated and unmodulated) is used with two separate reconstructors to estimate the atmospheric and piston segment modes, respectively.

In this paper, we propose employing an unmodulated six-sided prism wavefront sensor for estimating the piston segment modes on the EELT, in order to match the geometry of the prism to the geometry of the pupil, in particular, the six spider arms. We will investigate the sensitvity of the six-sided prism to piston segment modes for a six-arm spider by calculating the singular values of the interaction matrix formed for different relative angles of the prism edges to the spider arms, and calculate the error in reconstructing piston segment modes at different orientations.

The rest of this paper is structured as follows: in Section II, we will outline the theory behind the prism wavefront sensor class, the spider function geometry, and how we will calculate the piston segment errors. In section III, we will show the singular values and piston segment errors for different prism/spider geometries. Lastly, in Section IV, we will summarise and outline future work arising from the research in this paper.

II. BACKGROUND

The role of the wavefront sensor is to estimate the phase of the wavefront $\phi(x,y)$ at the aperture plane (x,y). This phase cannot be measured directly, but instead inferred from intensity measurements. The prism at the focal plane acts as a spatial filter $H(u,v)$, where (u,v) are the co-ordinates in the focal plane. The intensity measured at the detector $I(x,y)$ in the aperture plane after the re-imaging lens is given by [11]

$$I(x,y) \propto \left| \mathcal{F}^{-1}\left[H(u,v) \times \mathcal{F}\left[P(x,y)\exp[j\phi(x,y)] \right] \right] \right|^2, \quad (1)$$

where $\mathcal{F}$ and $\mathcal{F}^{-1}$ are the Fourier and inverse Fourier transforms respectively, $j = \sqrt{-1}$, and $P(x,y)$ is the magnitude at the aperture plane.

For the conventional 4-sided pyramid, the spatial filter $H_4(u,v)$ is given by

$$H_4(u,v) = \exp[j2\pi b(|u| + |v|)] \quad (2)$$

where b is the slope of the pyramid face, and determines the separation of the four images of the aperture at the re-imaged aperture plane. The phase of the spatial filter $H_4(u,v)$ for the pyramid is shown in Figure 5(a) and the resulting intensity images $I(x,y)$ at the conjugate aperture plane in Figure 6 (a) without atmospheric turbulence. The spatial filter for the six-sided prism $H_6(u,v)$ is calculated using the method of Engler *et al.* [18], and is shown in Figure 5(b). The correspnding intensity images $I(x,y)$ for the six-sided case are shown in Figure 6 (b), again with no wavefront aberration.
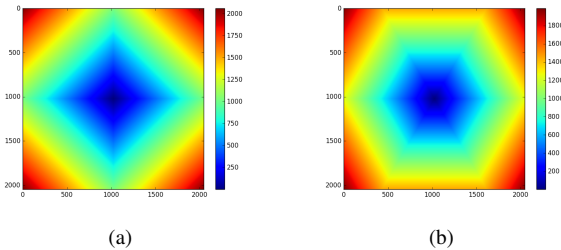

(a)   (b)

Fig. 5. The phase of the spatial filter $H(u,v)$ (radians) at the focal plane of the telescope introduced by (a) the pyramid wavefront sensor, and (b) the six-sided prism wavefront sensor. In both cases, the angle α of the prism edge to the x axis is 0°.

There are two principal methods for reconstructing the wavefront from the intensity images from a pyramid type WFS: reconstruction from slopes, and reconstruction from images [11]. The former takes linear combinations of the intensity images from geometric considerations to produce slope estimates in two orthogonal directions. Whereas in reconstruction from images, the interaction matrix is generated from the intensity images $I(x,y)$ themselves, and not from the slope estimates. Reconstruction from slopes has the advantage that the size of the interaction matrix is smaller, and is less affected by noise propagation than reconstruction from images. Reconstruction from images is more flexible, however, when we are dealing with a rotating prism, in that we do not need to
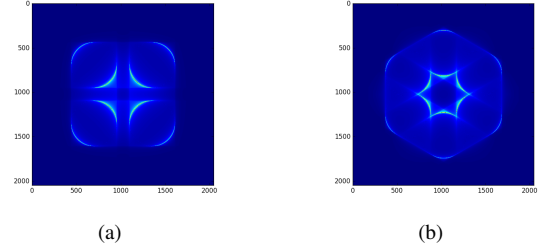

(a)   (b)

Fig. 6. The intensity image $I(x,y)$ formed with no wavefront aberration for (a) the pyramid wavefront sensor, and (b) the six-sided prism wavefront sensor. In both cases, the prism angle α is 0°, i.e. the edge of the pyramid is along the x axis.

recalculate the locations of the intensity images for each prism angle α. Instead, we can just use the entire $I(x,y)$ image. It is for this reason that in this paper we perform reconstruction from images.

For a pupil with M spider arms, there are M segment piston modes. We form the interaction matrix G for these segment piston modes by applying each of the M segment modes in turn to the DM and recording the intensity image $I(x,y)$, with each image forming a row of the interaction matrix

$$G = \begin{pmatrix} I_1(x,y) \\ I_2(x,y) \\ I_3(x,y) \\ \vdots \\ I_M(x,y) \end{pmatrix}. \quad (3)$$

Computationally, the segment modes, for example for M=6 as shown in Figure 3, are our $\phi(x,y)$ in Eq. 1.

We can calculate the eigenmodes and eigenvalues of the interaction matrix G with use of the singular value decomposition, such that

$$G = USV^T, \quad (4)$$

where the diagonal entries of matrix S are the square roots of the M eigenvalues or singular values of G, and U and V are unitary matrices.

In order to estimate the piston segment modes, we calculate a reconstruction matrix R based on the SVD decomposition (a pseudo-inverse)

$$R = VS'U^T, \quad (5)$$

where the diagonal of S' contains the reciprocal of the diagonal of S (reciprocal of the singular values). In this reconstruction process, we remove the global piston term (as it is weakly sensed) from the reconstruction by setting the Mth diagonal value of S'=0.

The estimate of the piston segment modes $\hat{a}$ can be calculated by

$$\hat{a} = RI(x,y), \quad (6)$$

where $I(x,y)$ is the measured image at the conjugate aperture plane. The error σ^2 in our reconstruction of the segment

piston modes is the sum of the squared difference between the segment piston modes a and their estimate $\hat{a}$

$$\sigma^2 = \sum_{m=1}^{M} (a - \hat{a})^2. \tag{7}$$

In the following section, we will calculate the eigenvalues and piston segment errors for a $N=6$ sided prism in conjunction with a $M=6$ arm spider for different rotation angles α of the prism relative to the spider.

III. RESULTS

For a pupil $P(x, y)$ with $M=6$ spider arms, the interaction matrix G has six non-zero eigenvalues. The eigenvalues give the sensitivity of the interaction matrix (measurements) to the associated eigenmode [16]. That is, a larger eigenvalue means the measurements are more sensitive to that mode, and it can be more easily estimated by the wavefront sensor. The eigenmodes are dependent on the relative orientation of the prism (angle α to x axis) to the pupil $P(x, y)$ spider arms (angle θ relative to the x axis). The singular values are the square of the respective eigenvalues.
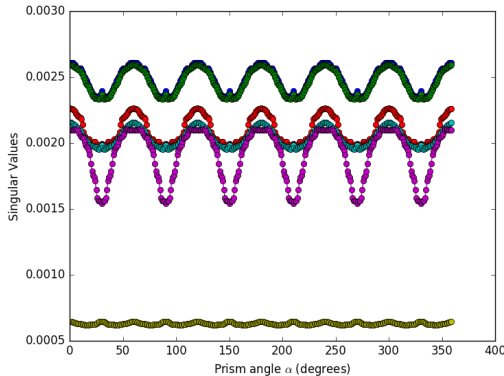

Fig. 7. The six singular values of the interaction matrix G versus the rotation angle α of the 6-sided prism for a six-arm spider with a rotation angle of 0°.

All the results in this section are presented for the parameter values listed in Table I, which are chosen to emulate the existing design values of the EELT. The aperture images

$I(x, y)$ are binned by a factor of 16 before being placed in the interaction matrix G.

In Figure 7, we plot the six singular values for a $M=6$ arm spider for a $N=6$ sided prism versus the angle α of the prism edge to the x axis. The spider arm angle is kept constant at $\theta = 0°$. The least sensitive eigenmode, which is shown in yellow, corresponds to piston. The sensitivity of this mode is largely unaffected by the angle of the prism relative to the spider arms. For the other five eigenmodes however, there is a clear dependence of the singular value (and consequently the eigenvalue) to the orientation of the prism relative to the spider arms.

For the five non-piston eigenmodes, the singular values (and consequently the eignevalues) are at a maximum at $\alpha = 0°$, and this repeats every 60°, equating to $\frac{360°}{N}$, where $M = N = 6$ here. Similarly, the singular values are at a minimum at 30°, and this repeats every 60°, equating to $\frac{360°}{N}$, where $M = N = 6$ here. In order to understand why these angles correspond to the maxima and minima, we need to consider Eq. 1. The intensity images are the inverse Fourier transform of the product of the prism spatial filter, $H(u, v)$, with the Fourier transform of the pupil function, including the spider arms, $P(x, y) \exp j\phi(x, y)$. The magnitude of the pupil function $P(x, y)$ consists of a circular pupil with central obscuration with spider arms as shown in Figure 8, for two different cases: one spider arm along the x axis (0°), and one with the spider arm at 30° to the x axis. The Fourier transform of the circular pupil provides the Airy disk pattern as the intensity image. The Fourier transform of each spider arm is a line orthogonal to the spider arm. Consequently, due to the the linearity property of the Fourier transform operator, the Fourier transform of $P(x, y)$ and therefore the intensity image, is the Airy disk with M diffraction spikes orthogonal to the arms of the spider. This is shown in Figure 9 for the two cases of $\theta=0°$ and 30°.
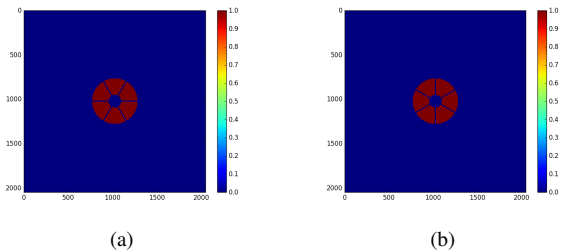

Fig. 8. The pupil magnitude function $P(x, y)$ for spider arms of angle θ of (a) 0° and (b) 30° of one arm to the x axis.

The six-sided sensor is least sensitive (smallest singular values) when the spider arms are at $\alpha = 30° + 60°n$, and consequently the diffraction spikes are at $\alpha = 0° + 60°n$. Thus the sensor is least sensitive when the diffraction spikes coincide exactly with the edges of the prism and this is shown in Figures 8(b) and 9(b). Conversely, the six-sided sensor is most sensitive when the diffraction spikes are in the middle of the pyramid faces, which is shown by Figures 8(a) and 9(a).
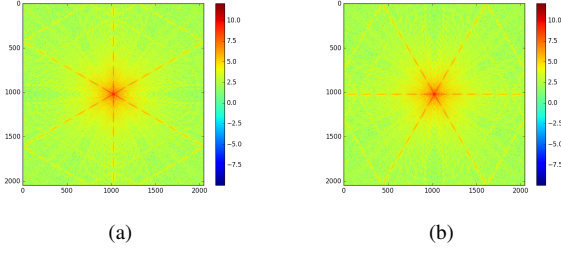
(a)   (b)

Fig. 9. The log of the magnitude of the Fourier transform of $P(x, y)$ for spider arms of angle θ of (a) $0°$ and (b) $30°$ of one arm to the x axis.

Ultimately to estimate the piston segment modes, we are interested in the sum of all of the M singular values of the interaction matrix G. In Figure 10, we plot the sum of the six singular values of G versus the angle of the prism relative to the x axis for a spider angle of $0°$. We see an almost perfect sinusoid with maxima at $0° + 60°n$ where the diffraction spikes due to the spider arms coincide with the prism edges, and minima at $30° + 60°n$ where the diffraction spikes are in the middle of the prism faces. The maximum sum of singular values is 15% larger than the minimum sum of singular values.
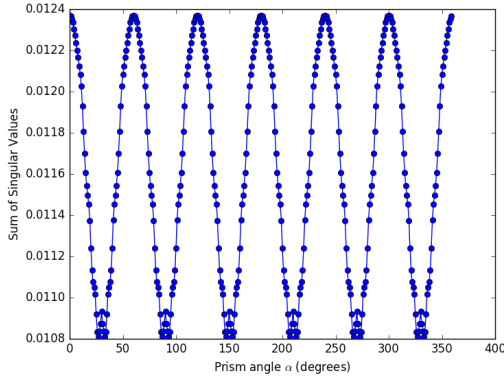

Fig. 10. The sum of the six singular values of the interaction matrix G versus the rotation angle of the N=6-sided prism for a M=6-arm spider with a rotation angle of $0°$.

To verify our hypothesis that for an M-arm spider and an N-sided prism, in the case $M = N$, the maxima of the singular values occurs when there is no overlap of the prism edge with the diffraction spike, we plot the cases of $M = N = 8$ and $M = N = 10$ in Figures 11 and 12 respectively. In both cases, the singular values exhibit sinuosoidal periodicity with period $360°/M$, and the maxima occur where there is no overlap of the diffraction spikes and prism edges, and the minima occur when there is full overlap of the diffraction spikes and prism edges.

We can determine the effect of this difference in sensitivity due to the orientation of the spider arms relative to the prism edges by calculating the piston segment error σ^2. For all angles, we apply a segment piston waffle mode of amplitude $\pi/8$ radian or 31 nm ensuring we are operating in a linear region of the sensor in a smaller manner to Ref. 14. The waffle
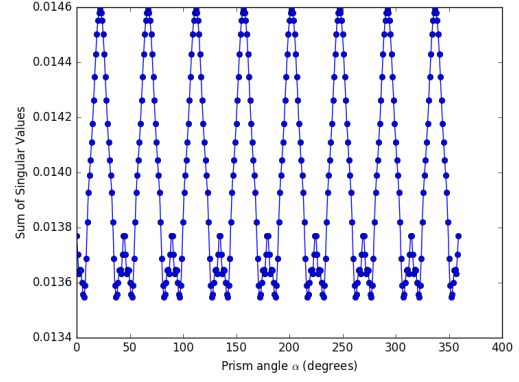

Fig. 11. The sum of the singular values of the interaction matrix G versus the rotation angle of the N=8-sided prism for a M=eight-arm spider with a rotation angle of $0°$.
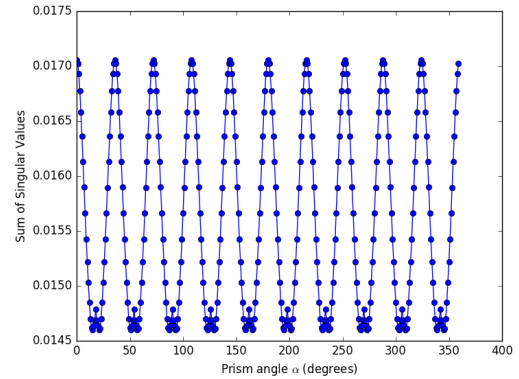

Fig. 12. The sum of the singular values of the interaction matrix G versus the rotation angle of the N=10-sided prism for a M=ten-arm spider with a rotation angle of $0°$.

mpde, which is shown in Figure 13, consists of alternating pushes and pulls of the six segments. We then use Eq.s 6 and 7 to calculate σ^2.

In Figure 14, we plot the error in the piston segment estimation σ^2 for the reconstruction of the waffle mode (alternating push and pull of the six segments) for $M = N = 6$. We see that the error is largest when the sensitivity as measured by the eigenvalues is lowest, and the error is smallest when the sensitivity is largest. The minima in the error occur when the diffraction spikes due to the spider arms fall in the middle of the prism faces, and the error is at its maxima when the prism edges align perfectly with the diffraction spikes due to the spider arms. The maximum error is 2.3 times larger than the minimum error. It should be noted that in this case we are simulating piston segment modes in the absence of any residual atmospheric turbulence and are assuming no photon or detector noise.

IV. CONCLUSIONS & FUTURE WORK

In this paper, we have shown that the sensitivity of the prism class of wavefront sensor to piston segment modes is
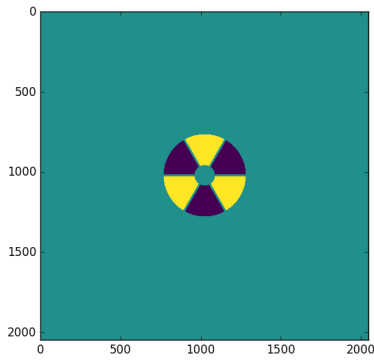
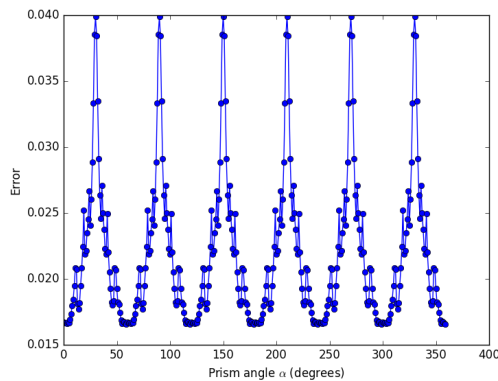Fig. 13. The waffle mode used to calculate the segment piston error.

Fig. 14. The segment piston error versus the rotation angle α of the 6-sided prism for a six-arm spider with a rotation angle of $\theta = 0°$.

dependent on the orientation of the prism edges relative to the spider arms. In particular, the six-sided sensor is most sensitive and provides the lowest error when the diffraction spikes due to the spider arms are in the middle of the prism faces. Conversely, the six-sided sensor is least sensitive to piston segment modes and yields the largest error when the diffraction spikes align with the edges of the prism faces.

In future work, we intend to estimate the piston segment modes in the presence of residual atmospheric turbulence and under realistic noise conditions. We will also investigate prisms with different number of sides, and spiders of different numbers of arms. Consequently, we will be able to see whether the six-sided prism is indeed the optimal geometry for the six-arm spider for the EELT.

REFERENCES

[1] P. Hickson, "Atmospheric and adaptive optics," *The Astronomy and Astrophysics Review*, vol. 22, pp. 22–76, 2014.
[2] R. Davies and M. Kasper, "Adaptive optics for astronomy," *Annual Review of Astronomy and Astrophysics*, vol. 50, no. 1, pp. 305–351, 2012.
[3] N. Hubin, B. L. Ellerbroek, R. Arsenault, R. M. Clare, R. Dekany, L. Gilles, M. Kasper, G. Herriot, M. Le Louarn, E. Marchetti, S. Oberti, J. Stoesz, J. P. Veran, and C. Vérinaud, "Adaptive optics for Extremely Large Telescopes," in *The Scientific Requirements for Extremely Large Telescopes* (P. Whitelock, M. Dennefeld, and B. Leibundgut, eds.), vol. 232 of *IAU Symposium*, pp. 60–85, Jan. 2006.
[4] C. Boyer, "Adaptive optics program update at TMT," Adaptive Optics for Extremely Large Telescopes 6, 2019.
[5] A. H. Bouchez, G. Z. Angeli, D. S. Ashby, R. Bernier, R. Conan, B. A. McLeod, F. Quirós-Pacheco, and M. A. van Dam, "An overview and status of GMT active and adaptive optics," in *Adaptive Optics Systems VI* (L. M. Close, L. Schreiber, and D. Schmidt, eds.), vol. 10703, pp. 284 – 299, International Society for Optics and Photonics, SPIE, 2018.
[6] H. Bonnet, F. Biancat-Marchet, M. Dimmler, M. Esselborn, N. Kornweibel, M. Le Louarn, P.-Y. Madec, E. Marchetti, M. Müller, S. Oberti, J. Paufique, L. Pettazzi, B. Sedghi, J. Spyromilio, S. Stroebele, C. Vérinaud, and E. Vernet, "Adaptive optics at the ESO ELT," in *Adaptive Optics Systems VI* (L. M. Close, L. Schreiber, and D. Schmidt, eds.), vol. 10703, pp. 327 – 335, International Society for Optics and Photonics, SPIE, 2018.
[7] R. Ragazzoni, "Pupil plane wavefront sensing with an oscillating prism," *Journal of Modern Optics*, vol. 43, pp. 289–293, Feb. 1996.
[8] C. Vérinaud, "On the nature of the measurements provided by a pyramid wave-front sensor," *Optics Communications*, vol. 233, no. 1-3, pp. 27–38, 2004.
[9] T. Y. Chew, R. M. Clare, and R. G. Lane, "A comparison of the Shack-Hartmann and pyramid wavefront sensors," *Optics Communications*, vol. 268, pp. 189 – 195, 2006.
[10] I. Shatokhina, A. Obereder, M. Rosensteiner, and R. Ramlau, "Pre-processed cumulative reconstructor with domain decomposition: a fast wavefront reconstruction method for pyramid wavefront sensor," *Appl. Opt.*, vol. 52, pp. 2640–2652, Apr 2003.
[11] R. M. Clare and R. G. Lane, "Wavefront sensing from spatial filtering at the focal plane," in *Astronomical Adaptive Optics Systems and Applications* (R. K. Tyson and M. Lloyd-Hart, eds.), vol. 5169, pp. 43 – 54, International Society for Optics and Photonics, SPIE, 2003.
[12] O. Fauvarque, B. Neichel, T. Fusco, J.-F. Sauvage, and O. Giraut, "A general formalism for Fourier based wave front sensing: application to the Pyramid wave front sensors," in *Adaptive Optics Systems V* (E. Marchetti, L. M. Close, and J.-P. Véran, eds.), vol. 9909, pp. 1741 – 1751, International Society for Optics and Photonics, SPIE, 2016.
[13] R. M. Clare, B. E. Engler, S. Weddell, I. Shatokhina, A. Obereder, and M. Le Louarn, "Numerical evaluation of pyramid type sensors for extreme adaptive optics for the European Extremely Large Telescope," Adaptive Optics for Extremely Large Telescopes 5, 2017.
[14] B. Engler, S. Weddell, M. Le Louarn, and R. Clare, "A flip-flop modulation method used with a pyramid wavefront sensor to correct piston segmentation on elts," *Journal of Astronomical Telescopes and Instrumentation Science*, submitted.
[15] B. Engler, S. Weddell, M. Le Louarn, and R. Clare, "Effects of the telescope spider on extreme adaptive optics systems with pyramid wavefront sensors ," in *Adaptive Optics Systems VI*, International Society for Optics and Photonics, SPIE, 2018.
[16] B. Engler, M. L. Louarn, C. Vérinaud, S. Weddell, and R. Clare, "Pyramid wavefront sensing in the presence of thick spiders," Adaptive Optics for Extremely Large Telescopes 6, 2019.
[17] V. Hutterer, I. Shatokhina, A. Obereder, and R. Ramlau, "Advanced wavefront reconstruction methods for segmented Extremely Large Telescope pupils using pyramid sensors," *Journal of Astronomical Telescopes, Instruments, and Systems*, vol. 4, no. 4, pp. 1 – 18, 2018.
[18] B. Engler, S. Weddell, and R. Clare, "Wavefront sensing with prisms for astronomical imaging with adaptive optics," in *2017 International Conference on Image and Vision Computing New Zealand (IVCNZ)*, pp. 1–7, 2017.